

# Evolution of the large-scale magnetic field on the solar surface: A parameter study

I. Baumann, D. Schmitt, M. Schüssler, and S. K. Solanki

Max-Planck-Institut für Sonnensystemforschung, 37191 Katlenburg-Lindau, Germany  
e-mail: baumann@linmpi.mpg.de

Received 5 April 2004 / Accepted 14 July 2004

**Abstract.** Magnetic flux emerging on the Sun's surface in the form of bipolar magnetic regions is redistributed by supergranular diffusion, a poleward meridional flow and differential rotation. We perform a systematic and extensive parameter study of the influence of various parameters on the large-scale field, in particular the total unsigned surface flux and the flux in the polar caps, using a flux transport model. We investigate both, model parameters and source term properties. We identify the average tilt angle of the emerging bipolar regions, the diffusion coefficient (below a critical value), the total emergent flux and, for the polar field, the meridional flow velocity and the cycle length as parameters with a particularly large effect. Of special interest is the influence of the overlap between successive cycles. With increasing overlap, an increasing background field (minimum flux at cycle minimum) is built up, which is of potential relevance for secular trends of solar activity and total irradiance.

**Key words.** magnetohydrodynamics (MHD) – Sun: magnetic fields – Sun: activity – Sun: photosphere

## 1. Introduction

The production and dissipation of the Sun's magnetic field is a complex process spanning the whole convection zone from the location of the solar dynamo at the tachocline near the base of the convection zone, over the transport of flux to the surface through buoyancy, to the evolution, dispersal and final cancellation of flux there. Of this combined problem we only consider the final part here, the evolution of the magnetic field at the Sun's surface.

New magnetic flux emerges at the solar photosphere in the form of bipolar magnetic regions (BMR) spanning a wide range of sizes (Harvey-Angle 1993). Statistical studies of the emergence patterns of BMRs show that new regions emerge at mid-latitudes at the beginning of a solar cycle and at low latitudes at the end of the cycle, leading to time-latitude plots that are commonly denoted as *butterfly diagrams*.

The dispersal of the magnetic flux of active regions was first considered by Leighton (1964) as a random-walk process of magnetic flux elements under the influence of the supergranular flow pattern. Flux transport models including differential rotation, diffusion (to account for this random walk) and a meridional flow have been developed by DeVore et al. (1985a), DeVore & Sheeley (1987) and Wang et al. (1989a) to describe the large-scale magnetic field by using observed source regions. More recently, flux transport models have been used to simulate the spreading of single bipoles (Mackay et al. 2002a; Wang et al. 2000) and whole activity cycles (Schrijver 2001; Mackay et al. 2002b). The latter authors used synthetic records of active regions. In most of the simulations, the model

parameters, i.e. diffusivity, meridional flow and differential rotation rate, have been adjusted in order to reproduce the observed surface magnetic field.

Here we investigate the influence of the transport parameters and also of the parameters governing the magnetic flux sources, i.e. location and strength of the emerging BMRs, on the evolution of the surface magnetic field with particular emphasis on the resulting total unsigned magnetic flux and the polar flux. The aim of the investigation is to understand how various parameters affect the transport of magnetic flux at the solar surface. This has applications for reconstructions of solar magnetic flux distributions over many cycles and will provide a guide for similar studies of surface fields on other late-type stars.

The paper is structured as follows. In Sect. 2 the flux transport model and its numerical realization is briefly described. In Sect. 3 the reference model (for the parameter study) and the analysing techniques for the large-scale magnetic field are presented. In Sect. 4 a wide range of parameters governing the flux transport model and their influence on the photospheric large-scale magnetic field are discussed. Finally, in Sect. 5 the conclusions drawn from the performed study are summarized.

## 2. Flux transport model

### 2.1. Transport equation

The magnetic field concentrated in the network and in active region plages is only weakly inclined relative to the vertical (Solanki 1993; Martinez Pillet et al. 1997), so that the

photospheric magnetic field can be taken as radially oriented (Wang & Sheeley 1992). Thus the flux transport of the large-scale magnetic field on the solar surface is described by the induction equation for the radial magnetic field component  $B_r(\theta, \phi, t)$  (Leighton 1964; DeVore et al. 1984; Sheeley et al. 1985). In spherical coordinates we have

$$\begin{aligned} \frac{\partial B_r}{\partial t} = & -\omega(\theta) \frac{\partial B_r}{\partial \phi} - \frac{1}{R_\odot \sin \theta} \frac{\partial}{\partial \theta} \left( v(\theta) B_r \sin \theta \right) \\ & + \frac{\eta}{R_\odot^2} \left[ \frac{1}{\sin \theta} \frac{\partial}{\partial \theta} \left( \sin \theta \frac{\partial B_r}{\partial \theta} \right) + \frac{1}{\sin^2 \theta} \frac{\partial^2 B_r}{\partial \phi^2} \right] \\ & + S(\theta, \phi, t). \end{aligned} \quad (1)$$

Here  $\theta$  is the colatitude,  $\phi$  is the longitude,  $R_\odot$  is the solar radius,  $\omega(\theta)$  is the angular velocity of the photospheric plasma,  $v(\theta)$  is the meridional flow velocity,  $\eta$  is the effective diffusion coefficient associated with the nonstationary supergranular motions and  $S(\theta, \phi, t)$  is a source term describing the emergence of new BMRs.

## 2.2. Transport parameters

One of the key ingredients in models of the type considered here is the diffusion coefficient. The model of Leighton (1964) required a diffusion coefficient in the range of  $770\text{--}1540 \text{ km}^2 \text{ s}^{-1}$  in order to reproduce the reversal of the polar fields during the sunspot cycle. Later, Mosher (1977) estimated the diffusion coefficient to lie in the range of  $200\text{--}400 \text{ km}^2 \text{ s}^{-1}$  by tracing the area covered by the magnetic field in active regions. This is roughly three times lower than the rate determined by Leighton. DeVore et al. (1985b) found the same range for the diffusion coefficient from simulations of the evolution of several observed active regions. Applying an average meridional flow with a flow amplitude of  $10 \pm 3 \text{ m s}^{-1}$  Wang et al. (1989b) constrained the diffusion coefficient to  $600 \pm 200 \text{ km}^2 \text{ s}^{-1}$  with the help of comparisons of numerical simulations with low-resolution, synoptic magnetic data. As the meridional flow speed they included is reasonable, the value of  $600 \text{ km}^2 \text{ s}^{-1}$  is adopted as reference value for the diffusion rate in the present study.

In the late 1970s first observational evidence for a poleward bulk flow was found. The highly concentrated polar fields during solar minimum supported the presence of a large-scale flow transporting magnetic field polewards. Duvall (1979) determined a flow amplitude of  $20 \text{ m s}^{-1}$  using observations of spectral line shifts. Topka et al. (1982) found an amplitude of  $10 \text{ m s}^{-1}$ . Due to possible interference between magnetic and Doppler signals large uncertainties remain Bogart (1987). For our simulations we use the meridional flow profile determined by Snodgrass & Dailey (1996) and Hathaway (1996),

$$v(\lambda) = \begin{cases} -v_0 \sin(\pi\lambda/\lambda_0): & \text{if } |\lambda| < \lambda_0 \\ 0 & \text{otherwise,} \end{cases} \quad (2)$$

where  $\lambda$  is the latitude in degrees ( $\lambda \equiv \pi/2 - \theta$ ) and  $\lambda_0$  is the latitude above which the meridional flow vanishes. We assume  $v_0 = 11 \text{ m s}^{-1}$  and  $\lambda_0 = 75^\circ$  as the *standard case*. This profile was also used by van Ballegooijen et al. (1998).

For the latitude-dependent differential rotation we assume the empirical profile of Snodgrass (1983)

$$\omega(\theta) = 13.38 - 2.30 \cos^2 \theta - 1.62 \cos^4 \theta \quad (3)$$

in units of  $\text{deg day}^{-1}$ .

## 2.3. Numerical treatment

For simulations of the photospheric magnetic field we have developed a two-dimensional code, denoted as SFTC (Surface Flux Transport Code). In order to integrate the flux transport Eq. (1), the radial magnetic field is expressed in terms of spherical harmonics. This simplifies the numerical treatment of the diffusion term to the well-known eigenvalue problem of the spherical Laplace operator. Furthermore, this method gives direct information on the evolution of the magnetic multipoles, especially the dipole component.

We consider all spherical harmonics between  $l = 0$  and  $l = 63$  for the expansion ( $l$  is the order of the spherical harmonics). This corresponds to a spatial resolution element roughly of the size of a supergranule ( $\approx 30 \text{ Mm}$ ). A higher spatial resolution would not be consistent with the model of turbulent diffusion.

We validated our code by reproducing previous results in the literature, including the evolution of a single bipole (Wang et al. 2000; Mackay et al. 2002b) and whole cycle simulations (Mackay et al. 2002b).

## 2.4. Description of a single newly emerged bipolar magnetic region

An emerging BMR adds its magnetic flux to the surface field. The initial distribution of the radial field is

$$\Delta B_r(R_\odot, \theta, \phi) = B_r^+(R_\odot, \theta, \phi) - B_r^-(R_\odot, \theta, \phi), \quad (4)$$

where  $B_r^\pm(R_\odot, \theta, \phi)$  are the unsigned distributions of the positive and negative polarity, respectively. We use the approach of van Ballegooijen et al. (1998), who represent a new BMR by two circular spots,

$$B_r^\pm(R_\odot, \theta, \phi) = B_{\text{max}} \exp \left\{ -\frac{2[1 - \cos \beta_\pm(\theta, \phi)]}{\delta_{\text{in}}^2} \right\}, \quad (5)$$

where  $\beta_\pm(\theta, \phi)$  are the heliocentric angles between  $(\theta, \phi)$  and the central coordinates of the positive and negative polarity,  $(\theta_\pm, \phi_\pm)$ , respectively. For small values of  $\beta_\pm$ , Eq. (5) approximates a Gaussian.  $\delta_{\text{in}}$  is the initial width of the Gaussian, which is assumed to be proportional to the angular separation,  $\Delta\beta$ , of the two active region spots:  $\delta_{\text{in}} = 0.4 \Delta\beta$ .  $B_{\text{max}}$  is set to  $250 \text{ G}$ . Note that in this way the only free parameters describing a newborn BMR are  $\theta_\pm$  and  $\phi_\pm$ . They determine the size and hence the total magnetic flux of the BMR. This description ensures that the fluxes in the positive and negative polarities of the newly emerged active region are always balanced.

Owing to the limited spatial resolution given by the numerical treatment (in particular, the restriction to  $l \leq 63$ ) very small BMRs cannot be resolved. We include the flux of such BMRs by considering them at a later stage of their development when

they have already diffused to a width  $\delta_0 = 4^\circ$ . This treatment means that we assume such regions not to cancel with magnetic flux from other sources prior to this time. The final description of the two polarities in the flux contribution of a newly emerged BMR to the photospheric magnetic field is therefore given by

$$B_r^\pm(R_\odot, \theta, \phi) = B_{\max} \left( \frac{\delta_{\text{in}}}{\delta_0} \right)^2 \exp \left\{ -\frac{2[1 - \cos \beta_\pm(\theta, \phi)]}{\delta_0^2} \right\}. \quad (6)$$

### 2.5. Simulating solar cycles

Simulations are carried out with a time step of one day. A weighted random number generator determines after every time step whether new BMRs appear on the model solar surface, where they appear, and which properties they have (see Sect. 3.1). The probability for a BMR to appear depends on the cycle parameters given as input and on the phase of the cycle. The new BMR described by Eqs. (4) and (6) is then added to the surface magnetic field and evolved according to Eq. (1).

The large-scale magnetic properties discussed below, e.g. the total unsigned photospheric field and the polar field strength, are taken as averages over the calculated cycles. Using this technique one has to be aware of the error resulting from statistical fluctuations. Because of the numerous parameter combinations examined in the study and the extended computing time needed we had to restrict the duration of the simulations to 55 years (two and a half magnetic cycles). For test purposes averages of many cycles have been calculated for some cases to ensure that the obtained results are reliable. Typical fluctuations of the large-scale magnetic field resulting from the random nature of the BMR properties do not exceed a few percent.

### 2.6. Initial field configuration

To start a simulation, an appropriate initial flux distribution is needed. For a given set of parameters, the initial field is chosen such that poleward meridional flow and equatorial diffusion approximately balance (van Ballegooijen et al. 1998),

$$v_0 B_r \approx \frac{\eta}{R_\odot} \frac{\partial B_r}{\partial \theta}. \quad (7)$$

This configuration corresponds to the situation at cycle minimum when only few BMRs emerge and the polar regions have maximal flux. The explicit form of the radial magnetic field results from Eqs. (2) and (7):

$$B_r(R_\odot, \lambda) = \begin{cases} \text{sign}(\lambda) B_0 \exp[-a_0(\cos(\pi\lambda/\lambda_0) + 1)] & \text{if } |\lambda| < \lambda_0 \\ \text{sign}(\lambda) B_0 & \text{otherwise,} \end{cases} \quad (8)$$

where  $\lambda$  is the latitude,  $\lambda_0 = 75^\circ$ ,  $a_0 = v_0 R_\odot \lambda_0 / (\pi \eta)$ ,  $\text{sign}(\lambda)$  is the sign of the latitude and  $B_0$  is the initial polar magnetic field strength, which has to be adjusted for each actual parameter set to avoid asymmetry of the global magnetic field with respect to the equator. The initial field given by Eq. (8) represents a situation where a new cycle is just about to start while the old decaying cycle is still ongoing due to an activity overlap set

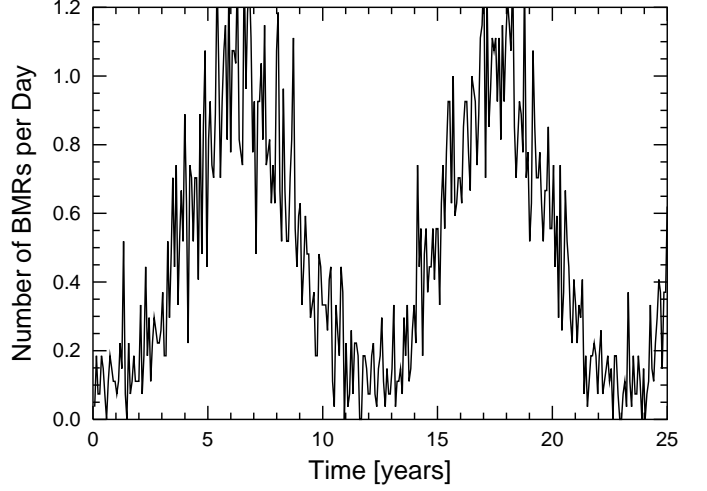


**Fig. 1.** The cycle activity for the reference parameter set. The number of BMRs emerging per day are averaged over 27 days.

to two years (see Sect. 3.1). Note that the initial radial field distribution is independent of longitude, i.e. it is axisymmetric.

## 3. Reference cycle model

### 3.1. Reference cycle parameters

To study the dependence of global magnetic properties on the cycle parameters, a reference case based on solar cycle parameters closely resembling the observed large-scale field evolution is defined. The length of each cycle is set to 13 years with an overlap time of two years between consecutive cycles. This overlap time is introduced on the basis of the work of Harvey (1992, 1993) and Hathaway et al. (1994), who showed that BMRs belonging to a new cycle start emerging while BMRs of the old cycle are still appearing. Note that due to this overlap the interval between two peaks of flux emergence is 11 years.

At the beginning of a cycle, BMRs emerge at a mean latitude of  $40^\circ$ , with a standard deviation of  $10^\circ$ . Towards the end of a cycle, the mean emergence latitude decreases to  $5^\circ$ , with a standard deviation of  $5^\circ$ . Emergence longitudes are assumed to be random, i.e. we neglect possible active longitudes. Unlike the true solar cycle which rises faster than it declines, the activity cycle in the simulation is represented by a Gaussian curve, i.e. it is symmetric around the time of maximum, which is reached 6.5 years after the beginning. Asymmetric cycles are studied in Sect. 4.10, where we find that asymmetry does not strongly affect the results. Figure 1 shows the number of BMRs emerging per day as a function of time. The corresponding butterfly diagram is plotted in Fig. 2. The angle of the BMR, i.e. the angle between the line connecting the two centres of the polarities and the east-west line, is taken according to Joy's law,  $\alpha = 0.5 \lambda$  ( $\lambda$  is the latitude). The polarity separations,  $\Delta\beta$ , of the simulated BMRs range from  $3.5^\circ$  to  $10^\circ$  in heliographic latitude with a step width of  $0.1^\circ$ . This corresponds to region sizes of 30 to 250 square degrees. Smaller regions or even ephemeral regions cannot be simulated, because of the limited numerical resolution. The assumed size distribution function

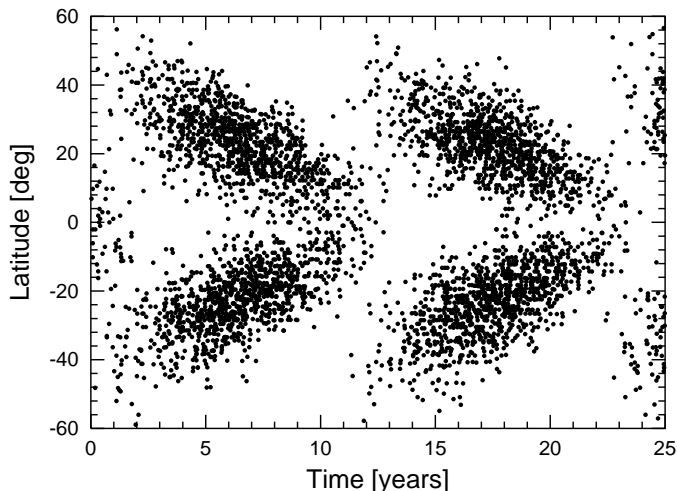


**Fig. 2.** Simulated butterfly diagram, latitudes of emerging active regions plotted vs. time, for the reference parameter set.

is  $n(A) \sim A^{-2}$ , where  $A$  is the area. This relation was found by Schrijver & Harvey (1994) through a power-law fit of the observed distribution of regions exceeding 3.5 square degrees in area. The biggest observed active regions in their study do not exceed 75 square degrees. For full-disk magnetograms excluding sunspots they yielded a linear relationship between the region size and its magnetic flux. The modelling of the active regions in the simulations as described above also leads to an almost linear relation between region size and flux content. The modelled BMRs are bigger in size than the ones emerging on the Sun. The larger areas in the simulations are necessary in order to account for the additional flux emerging in the ephemeral active regions, which are neglected in the current simulations. A value of  $B_{\max} = 250$  G in Eq. (6) leads to a smaller slope in the flux–area relation than found by Harvey, but ensures that the total number of roughly 2100 BMRs per cycle leads to a total input flux of approximately  $10^{25}$  Mx. A similar flux input of  $8.9 \times 10^{24}$  Mx per eleven-year cycle has been determined by Harvey & Zwaan (1993).

Figure 3 shows the magnetic butterfly diagram, i.e., a longitude-averaged time-latitude plot for the surface magnetic field, for the reference parameter set.

### 3.2. Unsigned magnetic flux

The total unsigned photospheric flux is obtained by integrating the radial field over the solar surface

$$\Phi_{\text{tot}} = R_{\odot}^2 \int |B_r(R_{\odot}, \theta, \phi, t)| dS. \quad (9)$$

Figure 4 shows the unsigned average flux density  $B_{\text{tot}} \equiv \Phi_{\text{tot}}/(4\pi R_{\odot}^2)$ , for the reference case. In the simulation, the field strength is calculated every 27 days. The fluctuations of the magnetic field make it hard to detect maxima and minima and compare them with the results for other parameter sets. Therefore the flux density is fitted using the nonlinear

least-squares Marquardt-Levenberg algorithm (Press et al. 1992). A sum of Gaussians is taken to start the fitting procedure

$$B_{\text{Fit}}(t) = \sum_1^N a_i \exp\left(\frac{-(t - b_i)^2}{e_i}\right), \quad (10)$$

where  $N$  is the number of maxima and  $a_i$ ,  $b_i$  and  $e_i$  are fitting parameters. The result of this fitting procedure is shown as the solid line in Fig. 4. The cycle maxima and minima given below are obtained by averaging over all extrema of the fitted curve for the simulated time series.

### 3.3. Polar fields

During solar minima, the polar fields reach their maximum values. The cycle of the Sun’s polar magnetic field is in antiphase to the Sunspot activity cycle. Svalgaard et al. (1978) derived an average polar cap field of 5 G during minimum and proposed an axisymmetric distribution of the large-scale field of the form  $B = \pm 11.5 \cos^2 \theta$  G. More recently, the Ulysses mission confirmed a polar field strength of 5 G (Smith & Balogh 1995). The polar field contributes strongly to the interplanetary and heliospheric field (open flux). Therefore, the evolution of the magnetic flux in the polar caps is an important quantity, but no unique definition of what constitutes the polar caps exists. In the literature, definitions for the solar polar caps range from the field within  $10^\circ$  of the pole to that within  $30^\circ$ . Figure 5 shows the calculated polar fields of the reference case for caps ranging in angular width from  $5^\circ$  to  $30^\circ$ . Apparently, the exact choice of this width does not have a strong effect on our results. We adopt a value of  $15^\circ$  for the polar cap in the remainder of the paper. In our analysis we are interested in the maximum values reached by the spatially averaged fields in these polar caps.

The maximum polar field strength is determined by averaging over the absolute values of all maxima and minima of both polar caps obtained during a simulation. To get the maximum values, the polar fields have been decomposed into their Fourier components. A few components turn out to be sufficient to well approximate the field and to remove noise. The different analysing technique compared with the fit procedure as used for the total surface field is necessary because the shape of the polar field is a priori not known in contrast to the total surface field, which follows approximately the shape of the cycle activity.

## 4. Parameter study: Results and discussion

For the study of the influence of the model parameters, i.e. diffusion coefficient, meridional flow amplitude and differential rotation rate, we use the same synthetic emergence sequence of BMRs in all calculations, while for the study of the cycle parameters new sequences of BMRs were created for each simulation.

Table 1 gives an overview of the parameters studied and the results of the corresponding simulation runs. Besides the description of the parameter (Col. 1), the value adopted for the standard case (Col. 2), and the range of values tested (Col. 3), we list the qualitative dependence of  $B_{\text{tot}}$  (Col. 4) and  $B_{\text{pole}}$  (Col. 5), the section in which this dependence is described as

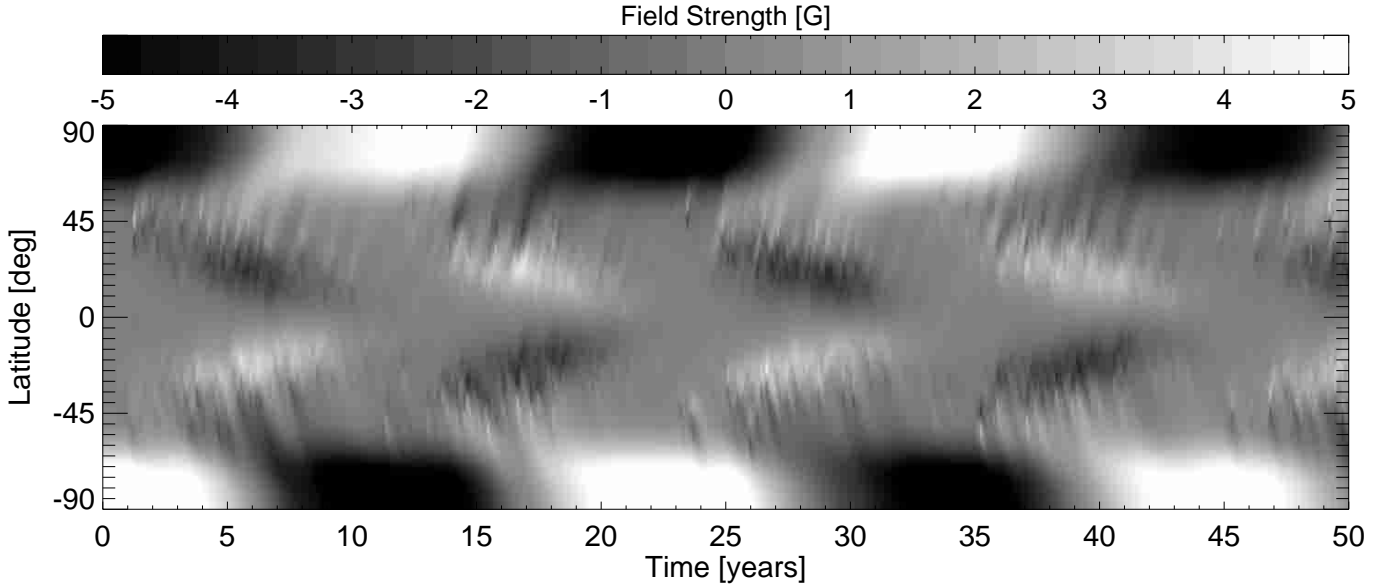


**Fig. 3.** Time-latitude plot of the surface magnetic field for the reference case. The magnetic field is averaged over longitude and over a time period of 27 days. The saturation level of the grey scale is set to 5 G (see bar at top).

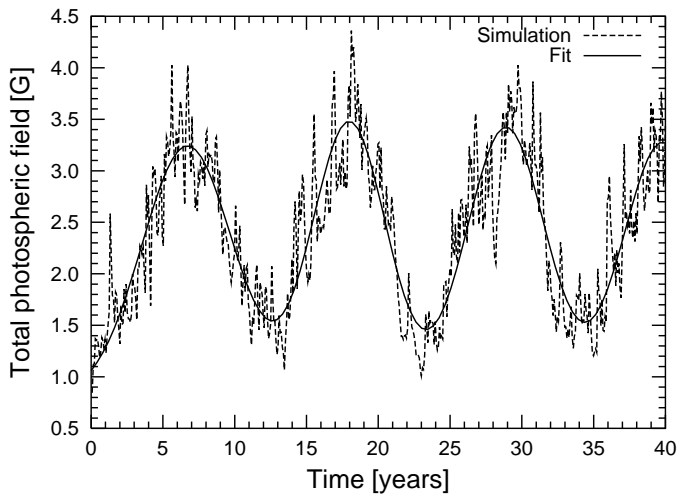


**Fig. 4.** Evolution of the total photospheric field (Eq. (9)) for the reference case. The total field is calculated every 27 days (dotted line). The solid line represents a nonlinear least-squares fit (Eq. (10)).

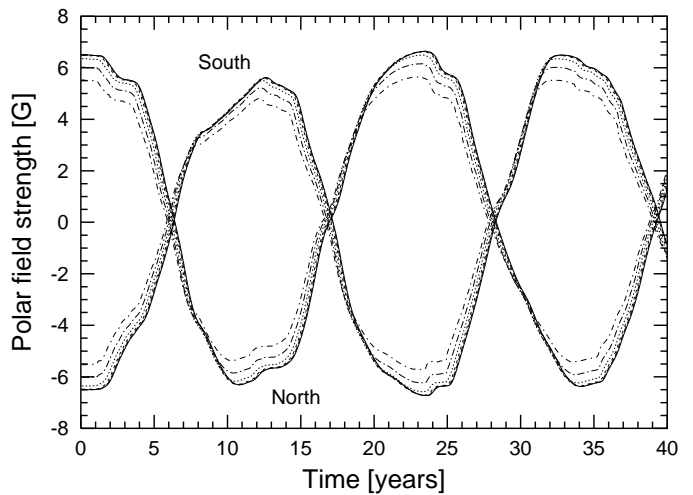


**Fig. 5.** North and south polar field calculated for sizes of the polar caps from  $5^\circ$  (largest field strength; solid curve) to  $30^\circ$  angular width (smallest field strength) in steps of  $5^\circ$ .

well as the number of the figure in which it is plotted (last column). The three parameters listed above the horizontal line are parameters of the model that enter into Eq. (1), while the remainder enters indirectly through the source term.

#### 4.1. Magnetic diffusivity

In order to obtain the dependence of the global magnetic field properties on the diffusion rate, simulations with diffusion coefficients in the range  $50\text{--}1500\text{ km}^2\text{ s}^{-1}$  have been run (the value adopted for the reference model is  $600\text{ km}^2\text{ s}^{-1}$ ). Figure 6a shows how the maximum and minimum magnetic surface fields,  $B_{\text{tot,max}}$  and  $B_{\text{tot,min}}$  respectively, vary with increasing diffusion coefficient. A higher diffusion rate leads to a faster spreading of the BMRs. Neighbouring magnetic

polarities approach each other faster than at a lower diffusion rate, leading to enhanced cancellation of flux and thus to the decrease in  $B_{\text{tot,max}}$  seen in Fig. 6a. This effect can be clearly seen in the magnetic butterfly diagrams for low ( $50\text{ km}^2\text{ s}^{-1}$ ) and high ( $1500\text{ km}^2\text{ s}^{-1}$ ) diffusion rates shown in Fig. 6c and Fig. 6d. In the first case meridional circulation dominates, carrying a large amount of flux to the poles, whereby early in a cycle the following polarity contributes more to the field being transported to high latitudes than later in the cycle. We expect that this due to Joy's law, with the tilt angles of BMRs being larger at high latitudes (i.e. early in the cycle).

The polar field shows a similar behaviour as the maximum of the total magnetic field (Fig. 6b). For a diffusion rate of  $50\text{ km}^2\text{ s}^{-1}$ ,  $B_{\text{pole}}$  is 14.5 G. This amplitude decreases rapidly

**Table 1.** Overview of the studied parameters and their influence on the total unsigned flux ( $B_{\text{tot}}$ ) and the polar field ( $B_{\text{pole}}$ ).

Parameter	Standard case	Range	Dependence of $B_{\text{tot}}$	Dependence of $B_{\text{pole}}$	Sect./ Fig.
Diffusion coefficient $\eta$ [ $\text{km}^2 \text{s}^{-1}$ ]	600	50–1500	Decrease	Strong increase; saturates for $\eta \gtrsim 500$	4.1/6
Meridional flow amplitude $v_0$ [ $\text{m s}^{-1}$ ]	11	0–30	Weak decrease	Reaches maximum at $v_0 = 8$	4.2/7
Differential rotation	$k = 1$	$k = 0 - 10$	Decrease	No effect	4.3/9
Activity level	1 (solar case)	0.2–10	Power-law	Linear increase	4.4/10
Cycle overlap [years]	2	0–6	Background forms for $B_{\text{tot,min}}$	Weak decrease	4.5 / 11
Cycle length [years]	13	5–20	Weak variation	Increase	4.6/12
Size distribution	$A^{-2}$	$A^{-p}$ , $p = 1-4$	Decrease	Weak decrease	4.7/13
Tilt angle	$0.5 \lambda$	$0.1 \lambda - 2.0 \lambda$	Linear increase	Linear increase	4.8/15
Scatter of tilt angles [deg]	0	0–30	No effect	No effect	4.8/ –
Shift of emergence latitudes [deg]	40	Initially 35–60	$B_{\text{tot,min}}$ decreases, $B_{\text{tot,max}}$ increases	Increase	4.9.1/17
Slope of mean emergence line [deg]	40/5 (start/ end of cycle)	22.5/22.5 to 45/0	No effect	Weak decrease	4.9.2/18
Spread around mean emergence line [deg]	10/5 (start/end)	0–20	No effect	No effect	4.9.3/ –
Position of activity maximum [years]	6.5 (= 0.5 cycle length)	1–12	No effect	No effect	4.10/ Table 2

with higher diffusion rates, and for  $\eta \approx 500 \text{ km}^2 \text{ s}^{-1}$  a saturation level of about 6 G is reached.

At still higher diffusion rates the enhanced cancellation of magnetic flux in the activity belts leaves less magnetic flux to migrate towards the poles. On the other side, a higher diffusion rate leads to more cross-equatorial cancellation of mainly preceding polarity flux. Both effects run contrary to each other and balance for high  $\eta$  so that  $B_{\text{pole}} \approx \text{const}$ .  $B_{\text{tot,min}}$  is mainly dominated by the polar field for high diffusion rates and thus shows a similar behaviour as  $B_{\text{pole}}$  for large values of  $\eta$ .

#### 4.2. Poleward meridional flow

We consider meridional flow velocities in the range  $0 \dots 30 \text{ m s}^{-1}$ . In the absence of a meridional flow ( $v_0 = 0$ ), most of the magnetic flux remains at low latitudes and the polar field extrema are about 3 G (Fig. 7b). However, magnetic flux transport only by diffusion is sufficient to reverse weak polar fields, as is clearly visible in the corresponding magnetic butterfly diagram (Fig. 7c), which shows rather diffuse fields at high latitudes, in contrast to the corresponding diagrams for reduced diffusion (Fig. 6c) or enhanced  $v_0$  (Fig. 7d). These latter show sharp stripes at high latitudes as flux from individual BMRs is transported to the poles, with the following polarity

dominating, but also including distinct stripes of the preceding polarity.

$B_{\text{pole}}$  as a function of  $v_0$  initially increases as more following polarity flux is carried to the poles. Also, an enhanced meridional flow reduces the diffusive dispersion of the polar fields. As  $v_0$  becomes even larger, cross-equatorial cancellation is reduced. Both magnetic polarities are carried to the pole by the meridional flow and cancel there. This leads to a reduction of  $B_{\text{pole}}$ . The strongest polar fields form for intermediate meridional flow speeds of  $v_0 = 8 \text{ m s}^{-1}$ .

A higher poleward meridional flow transports the opposite polarities to the smaller area in the polar regions, leading to more efficient cancellation and thus reduction of the total flux (Fig. 7a).

#### 4.3. Differential rotation

In this section, we modify the differential rotation (Eq. (3)) such that the rotation rate at the equator becomes  $k$ -times the solar value while the rotation rate at the poles remains at the solar value,

$$\omega_k(\theta) = [(k - 1)(\sin \theta + 1) - (k - 2)] \cdot \omega(\theta), \quad (11)$$

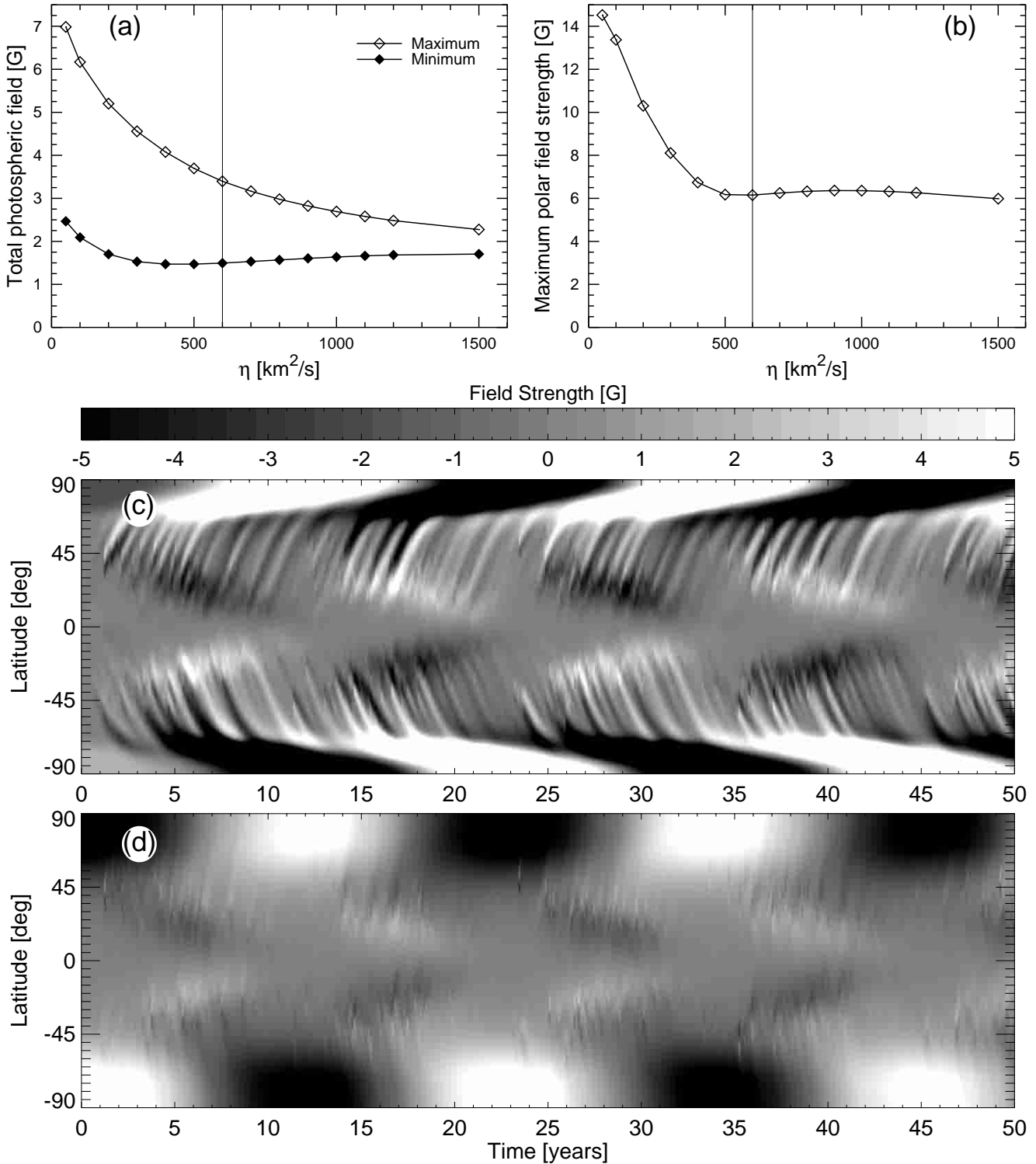


**Fig. 6.** **a)** Total photospheric field at cycle maximum ( $B_{\text{tot,max}}$ ) and minimum ( $B_{\text{tot,min}}$ ) vs. diffusion coefficient,  $\eta$ . The vertical line indicates the reference case. **b)** Polar field strength  $B_{\text{pole}}$  vs. diffusion constant,  $\eta$ . The plotted values are the averages of the absolute values of all maxima or minima. **(c, d)** Magnetic butterfly diagrams for the extreme values of the diffusivity:  $\eta = 50 \text{ km}^2 \text{ s}^{-1}$  **c)** and  $\eta = 1500 \text{ km}^2 \text{ s}^{-1}$  **d)**.

where  $\omega(\theta)$  is given by Eq. (3). The resulting rotation profiles are plotted in Fig. 8 for  $k = 1 \dots 10$ . The surface shearing due to differential rotation leads to flux cancellation by bringing opposite polarities together (see Figs. 2–4 in Mackay et al. 2002a). This effect is especially pronounced at mid latitudes and thus in the activity belts where a mixture of both polarities is present.

Figure 9 shows how  $B_{\text{tot}}$  decreases with increasing  $k$ . During cycle maxima the influence of the differential rotation on the total unsigned flux is significant. At minima, where only few BMRs are present and thus are more separated in longitude, a stronger differential rotation has only a weak effect on the total field.

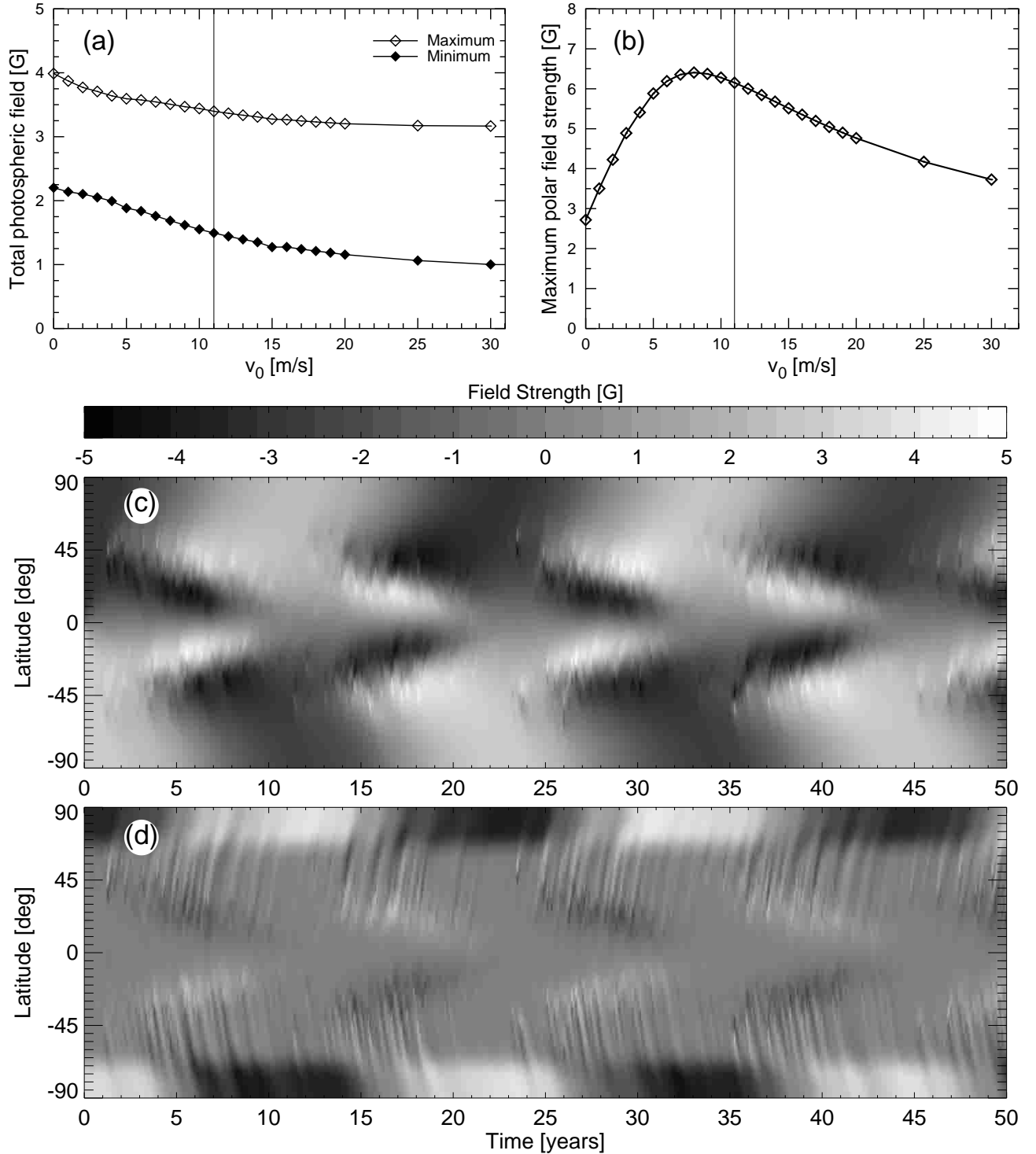


**Fig. 7.** **a)**  $B_{\text{tot,max}}$  and  $B_{\text{tot,min}}$  vs. meridional flow amplitude,  $v_0$ . The vertical line indicates the reference case. **b)** Polar field strength  $B_{\text{pole}}$  vs. flow amplitude. **(c), (d)** Magnetic butterfly diagrams for the extreme cases of absence of a poleward meridional flow **c)**, and for a meridional flow amplitude of  $v_0 = 30 \text{ m s}^{-1}$  **d)**.

The polar field is not influenced by differential rotation, which can be explained analytically: integrating the flux transport Eq. (1) over a circle of constant latitude from 0 to  $2\pi$  in longitude leads to a value independent of  $\omega(\theta)$ . For fixed values of the diffusion coefficient, the meridional flow and the source function, the average polar field is therefore independent of the

differential rotation with a value of  $B_{\text{pole}} = 6.2 \text{ G}$ , for all differential rotation profiles.

#### 4.4. Activity level

Next we consider the influence of changing activity level, i.e. total amount of emerging flux or cycle strength. This is relevant



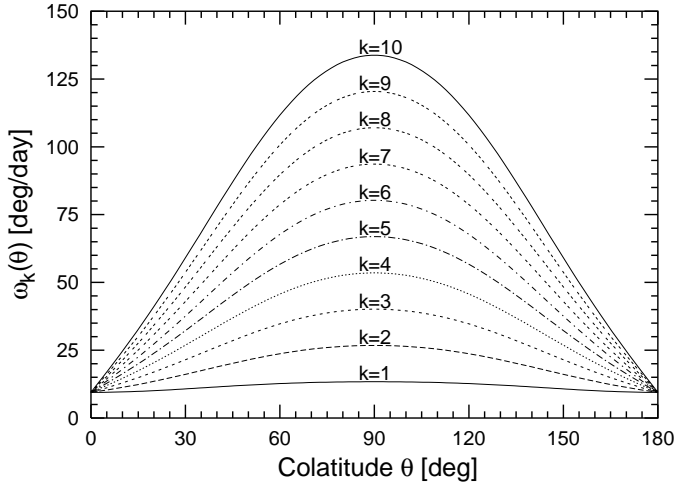


**Fig. 8.** Modified differential rotation profile vs. colatitude. The equator is assumed to rotate  $k$ -times faster than in the rotation curve of Snodgrass (1983), while the rotation at the poles is equal to the Snodgrass rotation, i.e. the standard case.

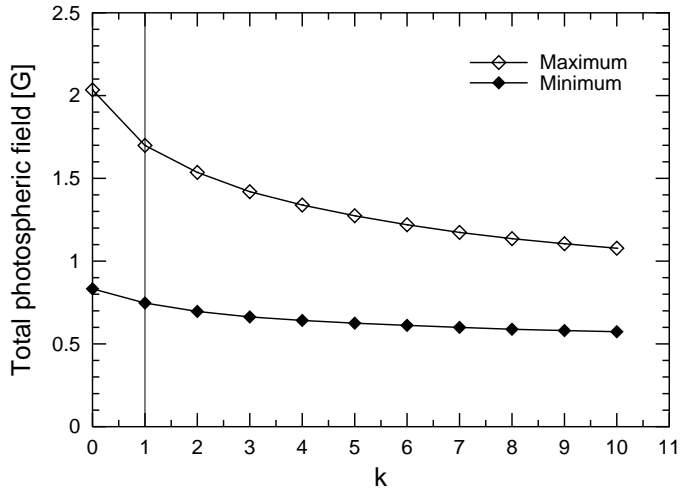


**Fig. 9.**  $B_{\text{tot,max}}$  and  $B_{\text{tot,min}}$  vs.  $k$  in the modified rotation profile (Eq. (11)).

for solar cycles of varying strength and for stars with different activity levels. We describe higher activity levels through a larger number of emerging BMRs and thus a larger amount of emerging flux while keeping the size distribution of emerging BMRs unchanged. To this end, we multiply the standard values  $N = 2100$  for the number of BMRs per cycle and  $\Phi_{\text{em,tot}} = 1.25 \times 10^{25}$  Mx for the total emerging magnetic flux both by a factor,  $C$ , where  $C = 1$  corresponds to the reference parameter set (solar case).

The simulation results are presented in Fig. 10a. Power-law fits (dotted and dashed lines in Fig. 10a) reveal the following dependence of the total surface field on the activity level:  $B_{\text{tot,max}} = 3.43 C^{0.73}$  G for cycle maxima and  $B_{\text{tot,min}} = 1.47 C^{0.88}$  G for cycle minima. Consequently, the total flux increases at a less than linear rate with increasing activity or emerging flux. As more BMRs emerge on the surface, opposite polarities emerge closer to each other, leading to more cancellation of magnetic flux. The larger exponent for  $B_{\text{tot,min}}$  probably

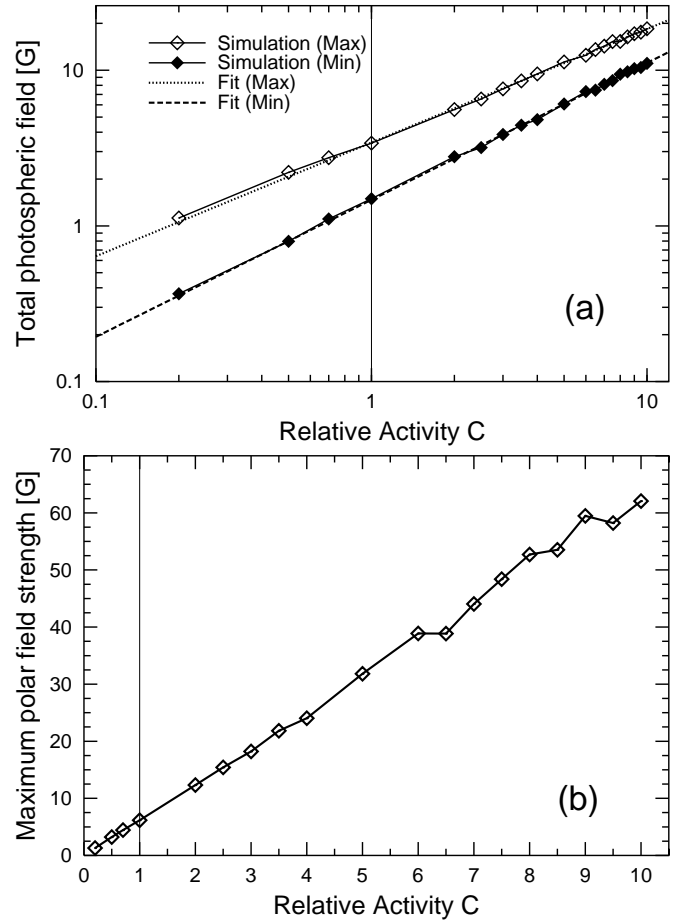


**Fig. 10.** **a)** Logarithmic plot of  $B_{\text{tot,max}}$  and  $B_{\text{tot,min}}$  vs. relative activity level  $C$  of cycle at its maximum and minimum. The fitted curves are also plotted. **b)**  $B_{\text{pole}}$  vs. the relative activity level of cycle.

arises from the fact that at activity minimum a significant fraction of the field resides in the polar caps, where a single polarity dominates.

The polar fields evolve linearly with the activity amplitude (Fig. 10b):  $B_{\text{pole}} = 6.15 C^{1.01}$  G from power-law fits. Similar results have been found by Schrijver & Title (2001). This behaviour is probably due to the fact that cross-equator flux cancellation also increases rapidly with activity level, so that the preferred transport of following-polarity flux to the poles is correspondingly enhanced.

Within the wide parameter range considered here, the surface evolution of the field does not lead to a saturation of  $B_{\text{tot}}$  or  $B_{\text{pole}}$ . The saturation of activity on very rapidly rotating stars (Vilhu & Rucinski 1983) is therefore probably not caused by cancellation of the magnetic field at the stellar surface. The power-law exponent of 0.73 between  $B_{\text{tot,max}}$  and emerging flux suggests that some contribution from this effect may be present, but it is not likely to dominate.

#### 4.5. Overlap time of successive cycles

In this section we study the influence of the overlap time of successive cycles, which is set to two years in the reference model. The length of the individual cycle remains at 13 years.

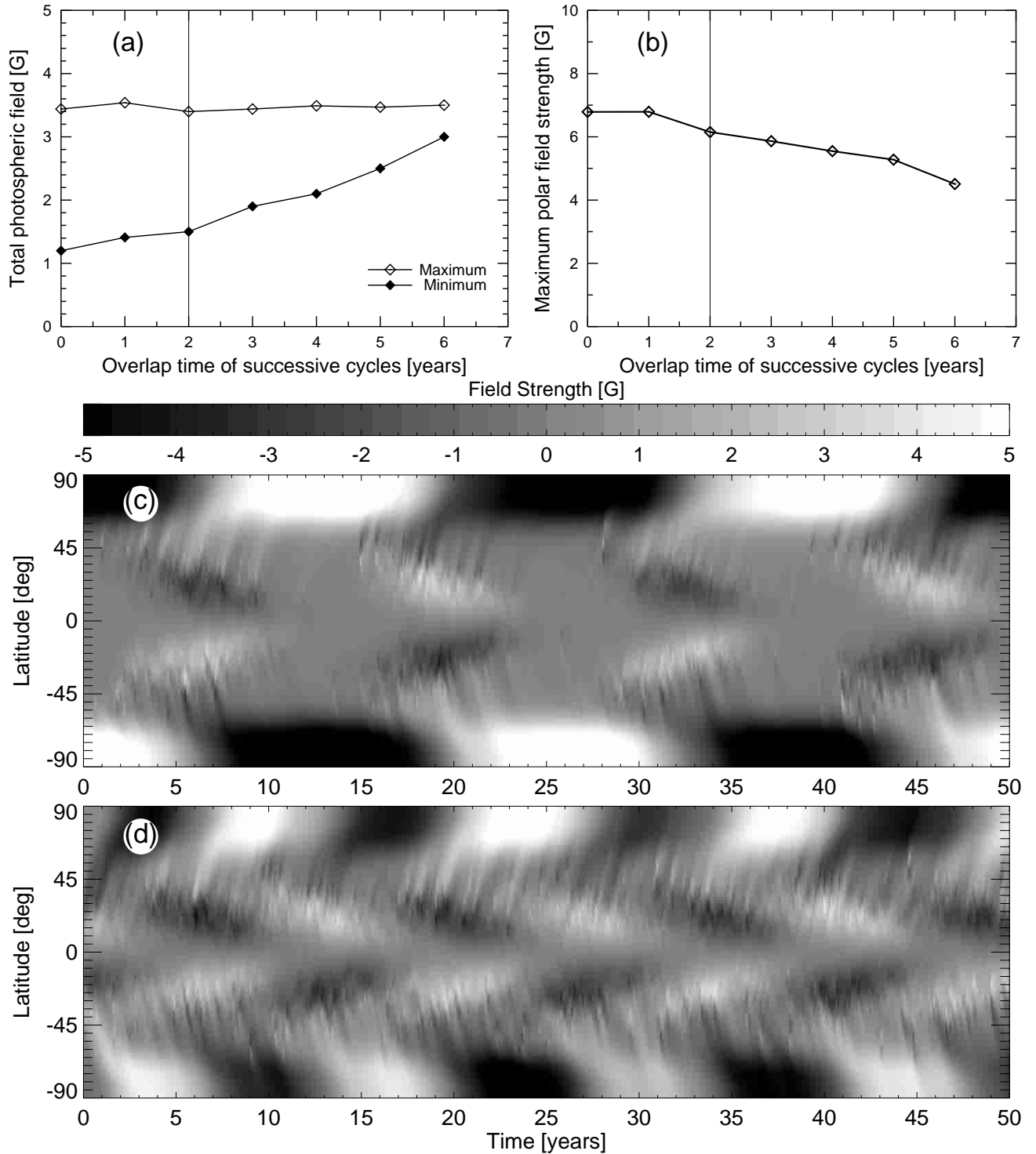


**Fig. 11.** a)  $B_{\text{tot,max}}$  and  $B_{\text{tot,min}}$  vs. overlap time of consecutive cycles. b) Polar field strength vs. overlap time. (c,d) Magnetic butterfly diagrams for no overlap between successive cycles c) and for an overlap time of 6 years d).

The simulations show that the surface flux during maxima is not influenced by varying the overlap time between 0 and 6 years (Fig. 11a). In contrast, the field during activity minima grows rapidly with the overlap between consecutive cycles. This result is in agreement with the predictions of the simple model describing the long-term evolution of the Sun's large-scale magnetic field by Solanki et al. (2000, 2002b) and

with the simulations of Schrijver et al. (1997). The growth of the field during minima can easily be understood by inspecting the butterfly diagram (Figs. 11c and d). For a large overlap (Fig. 11d), the simultaneous presence of two activity belts at high and low latitudes is clearly visible. In this extreme case for which the overlap time is half the cycle length, one cycle ends during the maximum of the following cycle and the

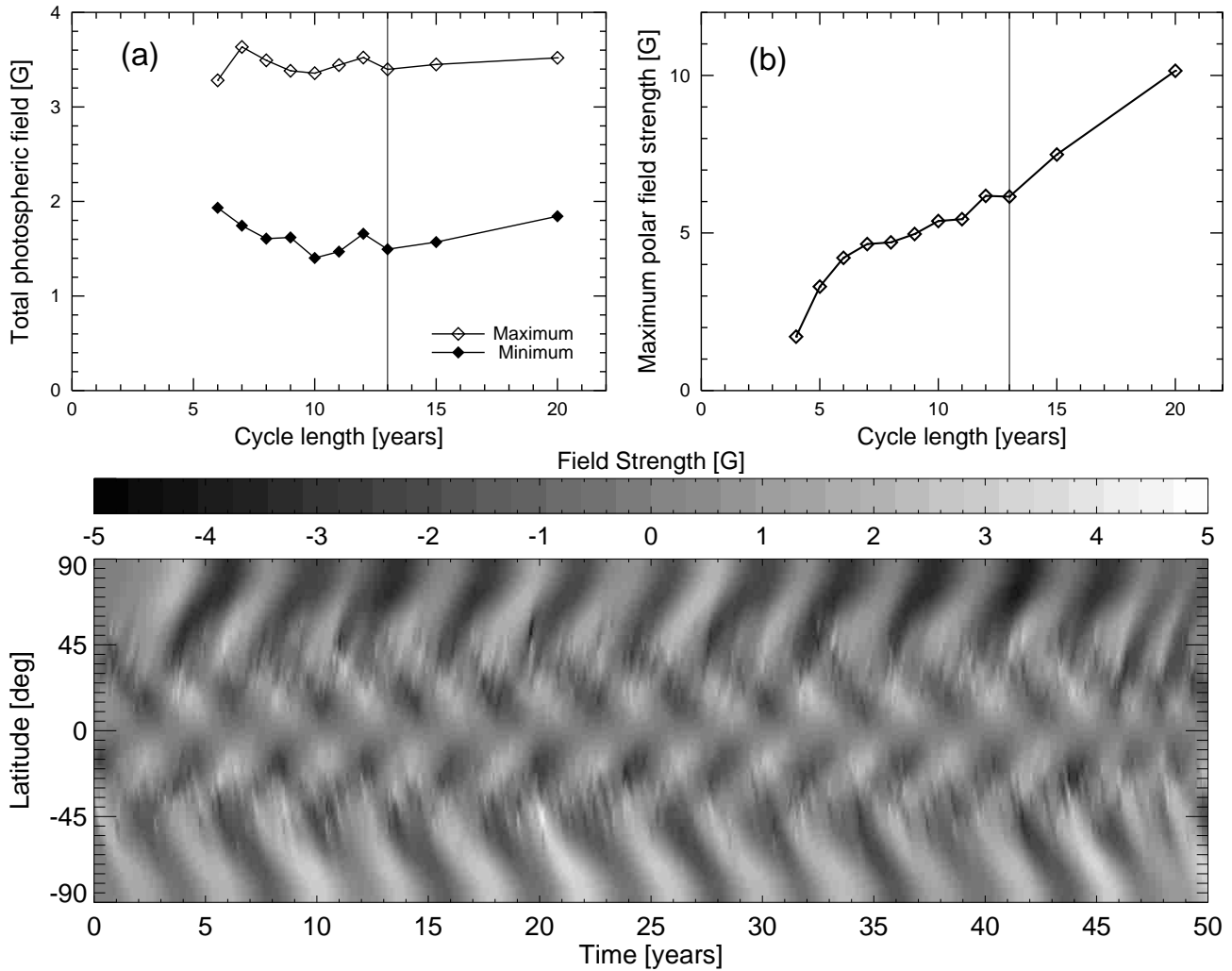


**Fig. 12.** a)  $B_{\text{tot,max}}$  and  $B_{\text{tot,min}}$  vs. cycle length. b)  $B_{\text{pole}}$  as a function of cycle length. c) Magnetic butterfly diagram for a cycle length of 5 years. The overlap time between successive cycles is 2 years.

photospheric flux no longer varies significantly with time (Fig. 11a). Thus the build-up of a background field by increasing the overlap time leads to a proportional decrease of the cycle amplitude.

For the polar fields, the effect of overlapping cycles corresponds to a decrease in the cycle length. The time during which magnetic flux is transported to the poles is reduced. The time between polar maxima decreases, with always the following-polarity flux from the cycle with higher emergence latitudes being at an advantage in reaching the poles. Therefore, the polar fields decrease with longer cycle overlaps (Fig. 11b). Why do cycles dominantly feed the polar flux during their early phases? We believe that this is due to a combination of effects. The emergence latitudes are higher and thus the tilt angles are larger during the initial phases. As we will see in Sects. 4.8 and 4.9, both of these parameters have a large effect on the polar fields.

#### 4.6. Cycle length

The length of the cycle has been varied from 4 to 20 years, keeping the overlap between two successive cycles always at a value of two years. The cycle amplitude was maintained at a

fixed level, so that the number of emerging BMRs varied linearly with the cycle length. The simulations show that the maximum total surface flux remains roughly constant (Fig. 12a) while  $B_{\text{tot,min}}$  displays a more complex behaviour. For short cycles (length  $\lesssim 10$  years)  $B_{\text{tot,min}}$  decreases with increasing length, while for longer cycles it increases gradually. The polar fields increase roughly linearly with the cycle period (Fig. 12b).

In a longer cycle, more BMRs emerge and contribute to the polar fields by preferential poleward transport of following-polarity. Since the cancellation of flux in the BMRs and between BMRs takes place on a timescale much shorter than the cycle length, the total flux is hardly affected by cycle length, at least at cycle maximum. The meridional flow becomes particularly important to keep the polar caps from diffusing away over longer cycles. Diffusion of polar flux could be one reason why in the case of the Sun, longer cycles tend to be followed by weaker cycles (Solanki et al. 2002a; Makarov et al. 2003).

The strong decrease of the polar field strength for short cycle periods is partly also due to the two-year overlap of successive cycles. The magnetic butterfly diagram (Fig. 12c) reveals that this enhances the decrease in the polar field at very short

cycles (see Sect. 4.5). The poleward flux transport is dominated by diffusion which results in weak polar fields (see Sect. 4.2). The very short duration of the phase in which one dominant polarity is being transported to the pole (stripes of one colour in Fig. 12c), means that over a considerable fraction of time opposite polarities are moving to the pole. Cancellation due to diffusion then reduces the polar flux. The decrease in  $B_{\text{tot,min}}$  with cycle period seen for short cycles is probably caused by the decreasing relative overlap between cycles as they get longer (compare Sect. 4.5). This effect is important for short cycles since the overlap in fraction of the cycle length is largest then.

#### 4.7. Size distribution of BMRs

Schrijver & Harvey (1994) determined the size distribution of solar active regions during cycle 21 as  $n(A) = 4.7 A^{-2}$ . An exponent of  $-2$  is a critical value, since for less negative exponents the new flux brought to the solar surface is dominated by the large active regions, while for more negative exponents it is the small ephemeral regions that dominate. We applied size distribution functions of the form  $n(A) \sim A^{-p}$  where  $p$  was varied between 1 and 4. In order to isolate the effect of the size distribution from other dependences, the total input flux from new regions was kept constant over the cycle by adjusting the total number of BMRs emerging over the cycle. For a higher value of  $p$  the probability of smaller regions increases and thus more regions have to emerge in order to reach a fixed amount of flux (Fig. 14).

The effect of the diffusion of the magnetic field and cancellation of magnetic flux is stronger in smaller active regions than in bigger ones. Therefore, the total surface flux is reduced when the distribution function is such that small regions are preferred (larger values of  $p$  in Fig. 13a). This effect is most pronounced at activity maxima when the largest number of active regions are present. At cycle minima a fair fraction of the flux is concentrated at the poles and thus less affected by the size distribution (see Fig. 13b), so that the total flux at minimum exhibits a weaker dependence on  $p$ . Field from bigger regions has a larger chance of reaching the polar caps owing to its longer lifetime (less cancellation due to diffusion) and thus the polar fields become stronger for lower values of  $p$  (Fig. 13b). The weak dependence of the polar fields on  $p$  can be explained by the same argument as for the dependence on the diffusion coefficient: more cancellation of flux in the activity belts is counterbalanced by increased cross-equatorial cancellation.

The dominance of the large BMRs for  $p = 1$  and of the small BMRs for  $p = 4$  is seen in the magnetic butterfly diagrams (Figs. 13c and d, respectively). The graininess of the field at both the emergence and higher (sub-polar) latitudes for  $p = 1$  contrasts with the smoothness (produced by averaging in the plot over many smaller regions) for  $p = 4$ . The upper panel looks more diffuse than the lower. The diffusion time  $\tau_d$  depends on the scale  $\tau_d = l^2/\eta$ , where  $l$  is a typical length and  $\eta$  is the diffusion coefficient, while the timescale for the meridional transport  $\tau_v$  does not ( $\tau_v = R_\odot/v_0$ ). If  $l$  decreases, i.e. when smaller BMRs are preferred, the diffusion becomes more important than the meridional flow.

Although  $B_{\text{pole}}$ , i.e. the maximal polar field strength, does not vary much with the size distribution, the temporal evolution of the polar fields changes as can be seen on the magnetic butterfly diagrams.

#### 4.8. Tilt angle

The tilt angle of a BMR,  $\alpha(\lambda)$ , is a result of the Coriolis force acting on the underlying toroidal magnetic flux tube as it rises to the surface. Starting from Joy's law,  $\alpha = 0.5 \lambda$ , we generalize the relation between tilt angle and latitude to  $\alpha = b \lambda$  and vary the parameter  $b$  between 0.1 and 2. Differences in the average tilt angle are expected to occur on stars of different spectral type, evolutionary status and rotation rate (activity level), since the strength of the Coriolis force relative to other forces acting on the rising flux tube depends on these parameters (Schüssler & Solanki 1992; Schüssler et al. 1996).

$B_{\text{tot,max}}$  shows a linear increase with  $b$  (Fig. 15a). For larger tilt angles, opposite polarities from neighbouring BMRs are more separated in longitude and thus diffusion is less effective in flux cancellation. For larger tilt angles, cross-equatorial cancellation of preceding flux is enhanced (see the evolution of a single bipole described in Mackay et al. 2002a), leading to more flux on the solar surface and at the same time also to the accumulation of more flux at the poles. Thus the polar fields become stronger for higher values of  $b$  (Fig. 15b). In the investigated range of  $b$ , the polar field strength is approximately  $B_{\text{Pole}} \approx 12 b$ ,  $B_{\text{tot,max}} \approx 1.8 b + 2.6$  and  $B_{\text{tot,min}} \approx 1.6 b + 0.7$  (all values in G).

We have also considered the influence of a scatter in the tilt angles. The standard deviation of the tilts of individual BMRs around the mean is  $\sim 19^\circ$  (Wang & Sheeley 1989). We have considered random distributions of tilt angles with standard deviations ranging from  $1^\circ$  to  $30^\circ$ . It turned out that this had no significant effect on both the total magnetic field and the polar field as long as average tilt angles were kept constant. The total fluxes at activity maximum and minimum varied by less than 10% over the considered parameter range, while the polar field varies by less than 30%. Both quantities did not show a clear trend.

#### 4.9. Emergence latitudes

A quantitative analysis of the influence of the emergence latitudes of the BMRs on the global field properties has been performed for two cases (see Fig. 16). In the first case, we have shifted the entire activity belt in latitude, while in the second case we have changed the range of emergence latitudes while keeping the average emergence latitude of all BMRs in a cycle fixed. This corresponds to changing the slope of the mean emergence line in the butterfly diagram. In order to obtain clear trends, the width of the distribution around the mean emergence line has been set to  $\sigma = 1^\circ$ . Subsequently, the spread  $\sigma$  around the mean latitudes has also been varied.

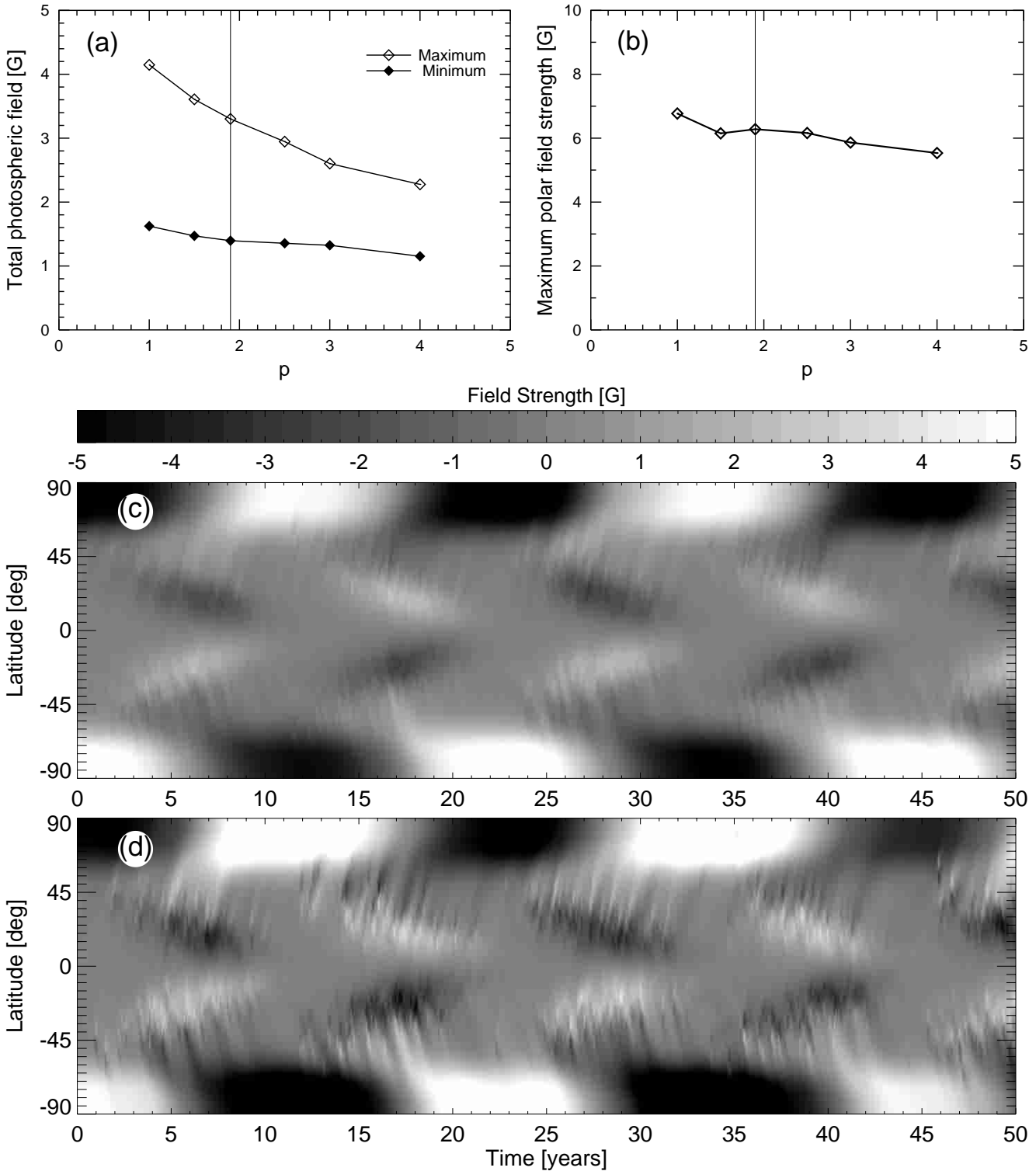


**Fig. 13.** **a)**  $B_{\text{tot,max}}$  and  $B_{\text{tot,min}}$  vs. exponent  $p$  in the size distribution function  $n(A) \sim A^{-p}$ . **b)** Polar field strength vs.  $p$ . **(c,d)** Magnetic butterfly diagrams for size distributions of active regions  $\sim A^{-4}$  **c)** and  $\sim A^{-1}$  **d)**.

#### 4.9.1. Shift of the emergence latitudes (case 1)

A poleward shift of the activity belt in general leads to higher polar field strengths (Fig. 17b). The BMRs emerge closer to the pole and thus the time for reaching it by diffusion and meridional advection is shorter and therefore cancellation through diffusion is reduced. Also, higher emergence latitudes result in

higher tilt angles of the BMRs which lead to a higher  $B_{\text{pole}}$  (see Sect. 4.8). A slight increase in the polar field is given when the activity belt is shifted equatorwards relative to the standard case. In this case, diffusion over the equator enhances cancellation of leading polarity, and increasing distance from the equator decreases this cancellation.

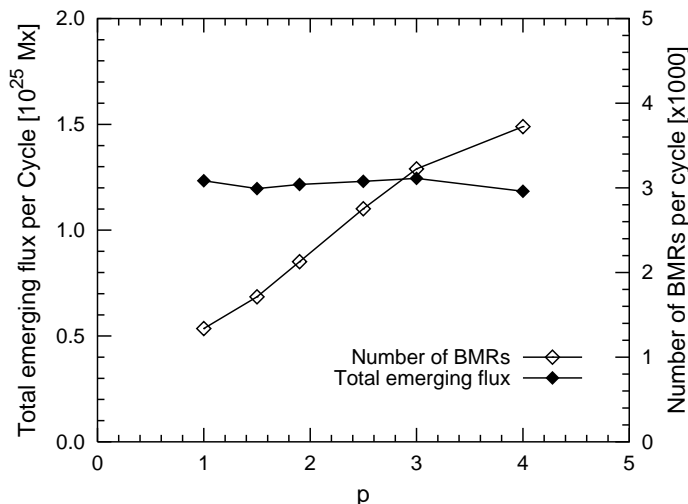


**Fig. 14.** Number of emerging BMRs per cycle and total emerging flux per cycle vs. the exponent  $p$  in the size distribution function  $n(A) \sim A^{-p}$ . The total number of emerging BMRs in the individual simulations is set such that the total emerging flux remains roughly constant.

The total surface field exhibits a stronger contrast between cycle maximum and minimum with increasing emergence latitude (Fig. 17a). At cycle maximum increasing latitude of emergence decreases the amount of cross-equatorial cancellation between leading polarities, leading to a larger amount of flux at maximum. This effect is most important as long as emergence latitudes are small. But why is there less field at minimum? Possibly: with less cross-equator cancellation more cancellation between fluxes in the same hemisphere takes place ( $B_{\text{tot,min}}$  is like a mirror of  $B_{\text{tot,max}}$ ).

#### 4.9.2. Range of emergence latitudes (case 2)

Changing the slope of the wings of the butterfly diagram leaves the average tilt angle of the BMRs unchanged, thus not having a strong effect on the surface field (Fig. 18a) and also not on the polar fields (Fig. 18b). The difference in the field strength between the extreme cases, e.g. constant emerging latitudes over the cycle and a strong decrease from  $\theta_{\text{in}} = 45^\circ$  at the beginning to  $\theta_{\text{fi}} = 0^\circ$  at the end of the cycle, is only about 3 G for the polar field. This indicates that the two effects described in the previous paragraph, e.g. fast approach of the poles for polarities emerging at high latitudes and high diffusion across the equator for flux emerging at low latitudes, roughly compensate. Cancellation in the polar region reduces the polar field, while cancellation across the equator supports a higher polar field.

#### 4.9.3. Spread around the mean (case 3)

Both the total surface field and the polar fields are remarkably independent of the statistical spread of BMRs around the mean. There is no noteworthy change in the field strengths ( $<10\%$ ) if the standard deviation is increased from 0 to  $20^\circ$ .

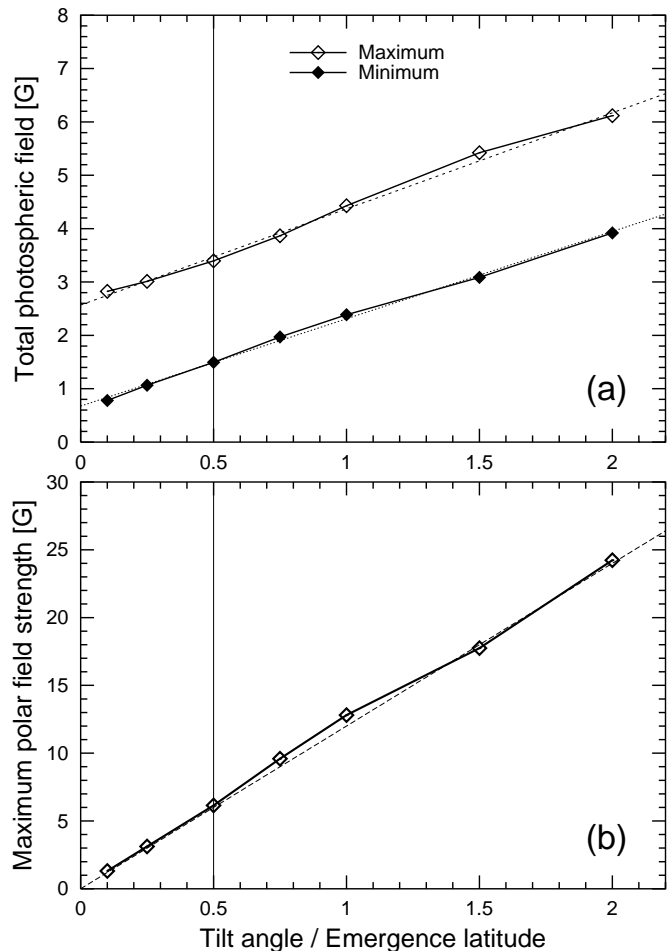


**Fig. 15. a)**  $B_{\text{tot,max}}$  and  $B_{\text{tot,min}}$  vs. parameter  $b = \alpha/\lambda$  ( $\alpha$  is the tilt angle and  $\lambda$  is the emergence latitude). **b)** Polar field strength vs.  $b$ . The linear fits are also indicated.

#### 4.10. Asymmetric activity cycles

In the previous sections, the simulated activity cycle was always symmetric in time with respect to the cycle maximum. However, the sunspot record shows that the solar maximum is reached already well in the first half of most cycles. In order to study asymmetric cycles we have considered the following class of time profiles of flux emergence: a linear increase until the maximum followed by a linear decrease to zero. The corresponding emergence rates of BMRs have been adjusted such that the total number of BMRs during a cycle remains constant and equal to the previously used Gaussian profile. The times of activity maxima can now be varied between 1 and 12 years after the beginning of a cycle. It turns out that the total surface field as well as the maximum value of the polar field do not depend significantly on the time of the cycle maximum. Both quantities vary by less than 15%. Figure 19 shows the polar field strength for the case when the activity maximum is reached after 2 and after 11 years, respectively. In the first case, the high initial emergence rate coupled with the large tilt and high emergence latitude of the BMRs early in the cycle leads to an early polar reversal and a fast build-up of the polar fields. The new maximum of  $B_{\text{pole}}$  is built up within 3 years. After the maximum of the emergence rate, the amount of net flux reaching

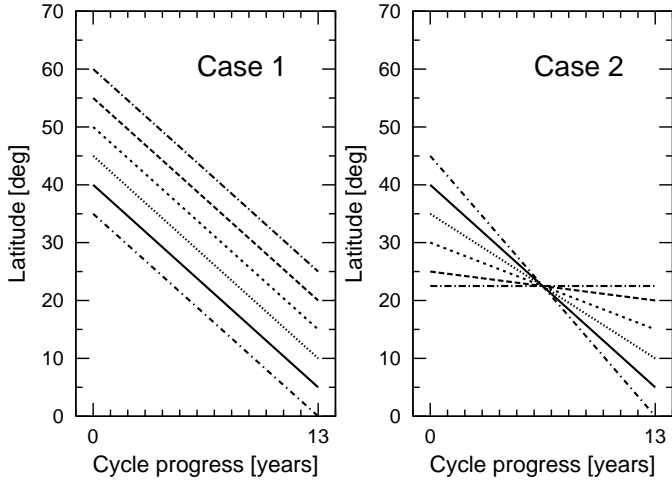


**Fig. 16.** Sketch of the variation of the mean activity line in the butterfly diagram. *Left:* the mean line is shifted, with starting latitudes ranging from 35 to 60° (case 1). *Right:* variation of the slope of the mean activity line (case 2). The solid line represents the reference case.

the poles decreases rapidly as both the emergence rate and the tilt angles of the BMRs decrease. It appears to be just sufficient to maintain the polar field, which leads to a roughly rectangular time profile of the polar fields. In contrast, when the activity peaks very late in the cycle, i.e. at low latitudes, the polar field reversal takes place over a longer period of time resulting in a sharp maximum of polar field strength.

#### 4.11. Shape of activity profile

Except for the last section, the activity profile was taken to be Gaussian in shape. Here we consider the influence of the functional form on the global field by comparing three different types of activity profiles. Alternatively to the Gaussian profile we apply a linear form of activity as described in the preceding section with the maximum in the middle of the cycle as well as a sinusoidal one. The total amount of BMRs per cycle, i.e. the amount of emerging flux integrated over the activity curve for one cycle, is held constant. Table 2 shows  $B_{\text{tot}}$  and  $B_{\text{pole}}$  for the three cases.

A linear increase and decrease of the activity leads to smaller  $B_{\text{tot,max}}$  and higher  $B_{\text{tot,min}}$  compared with the Gaussian profile. In the latter case, the cycle maximum is wider than in the linear case, which explains the higher  $B_{\text{tot,max}}$ . In contrary, during cycle minimum, where an overlap of two cycles is present, the superposition of two linear cycle activities is larger for the linear profile than for the Gaussian profile, for which the overlap of two cycles nearly vanishes.

The sinusoidal profile gives an emergence pattern in between the two other discussed cases, so that  $B_{\text{tot,max}}$  and  $B_{\text{tot,min}}$  have intermediate values.

The polar field does not vary significantly with the shape of the profile in all three cases.

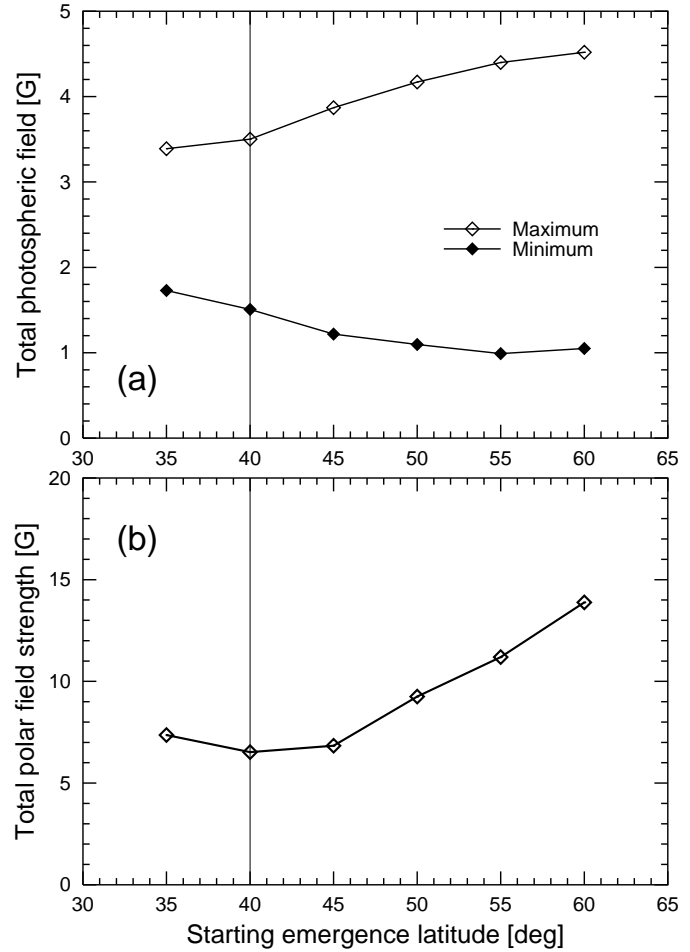


**Fig. 17.** a)  $B_{\text{tot,max}}$  and  $B_{\text{tot,min}}$  vs. starting mean emergence latitude. b) Polar field strength vs. starting latitude.

**Table 2.** Dependence of the total field and the polar field on the functional form of the activity cycle.

activity profile	$B_{\text{tot,max}}$ [G]	$B_{\text{tot,min}}$ [G]	$B_{\text{pole}}$ [G]
Gaussian	3.4	1.5	6.2
Linear	2.6	1.9	5.5
Sinusoidal	2.9	1.8	5.0

#### 4.12. Phase relation between the activity cycle and polar fields

The polar fields reverse around cycle maximum. A more precise determination of the time lag between BMR emergence rate and polar field reversal can be obtained by shifting and crosscorrelating both time series. The maximum correlation coefficient indicates the phase difference. This method has been applied to all of the above discussed parameter sets. It turns out that for all cases the polar fields reverse within  $\pm 0.5$  years of cycle maximum.

## 5. Conclusion

We have considered the large-scale evolution of the magnetic field arising from the flux transport model for a variety of

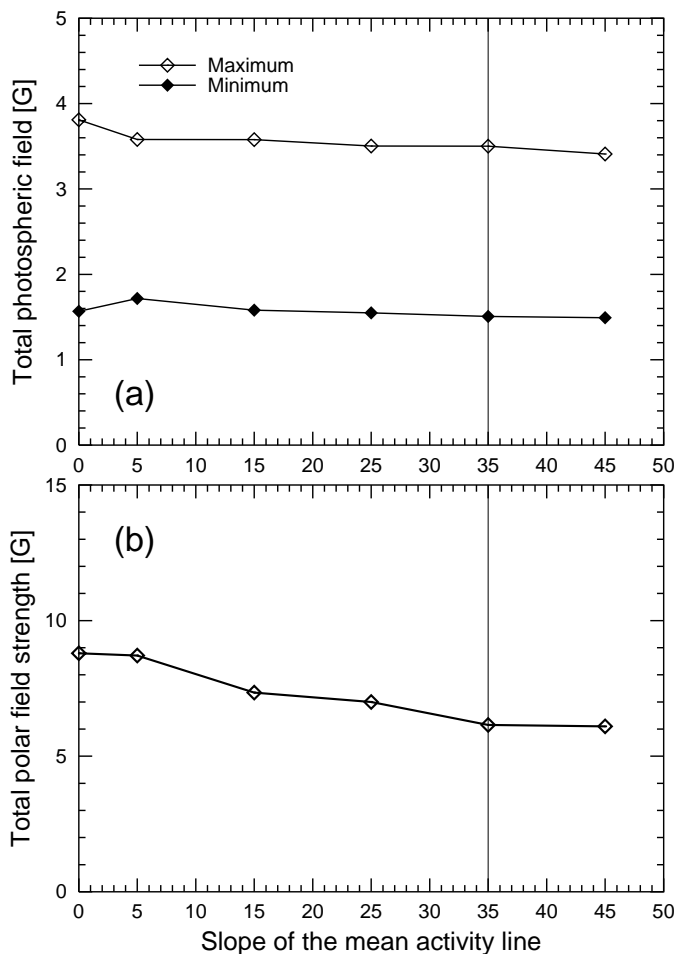


**Fig. 18.** **a)**  $B_{\text{tot,max}}$  and  $B_{\text{tot,min}}$  vs. slope  $\theta_{\text{in}} - \theta_{\text{fi}}$  of the mean activity line at cycle maximum and minimum. **b)** Polar field strength vs. slope of the mean activity.

parameters. Two types of parameters can be distinguished: model parameters, i.e. diffusion coefficient, meridional flow and differential rotation, which influence the flux transport, and parameters that influence the source term in Eq. (1). The latter control the emergence rate, emergence latitudes and emergence time of new BMRs. We have carried out a detailed study of the dependence of relevant properties on the large-scale surface field on these parameters. This has helped us to distinguish the parameters having a large influence on global magnetic properties from those playing a smaller role. The average tilt angle of the BMRs, the diffusion coefficient and the activity, e.g. the total emergent flux, have a particularly large effect on the polar field and the total unsigned flux. The meridional flow velocity and the cycle length have a large influence on the formation of the polar field. The overlap time of consecutive cycles leads to the formation of a background field (field during cycle minimum).

The parameter study should help in particular to get a better understanding of the behaviour of the large-scale field on the Sun at different times and at different activity levels. We also expect it to provide a guide for future studies of the magnetic field evolution on cool stars.

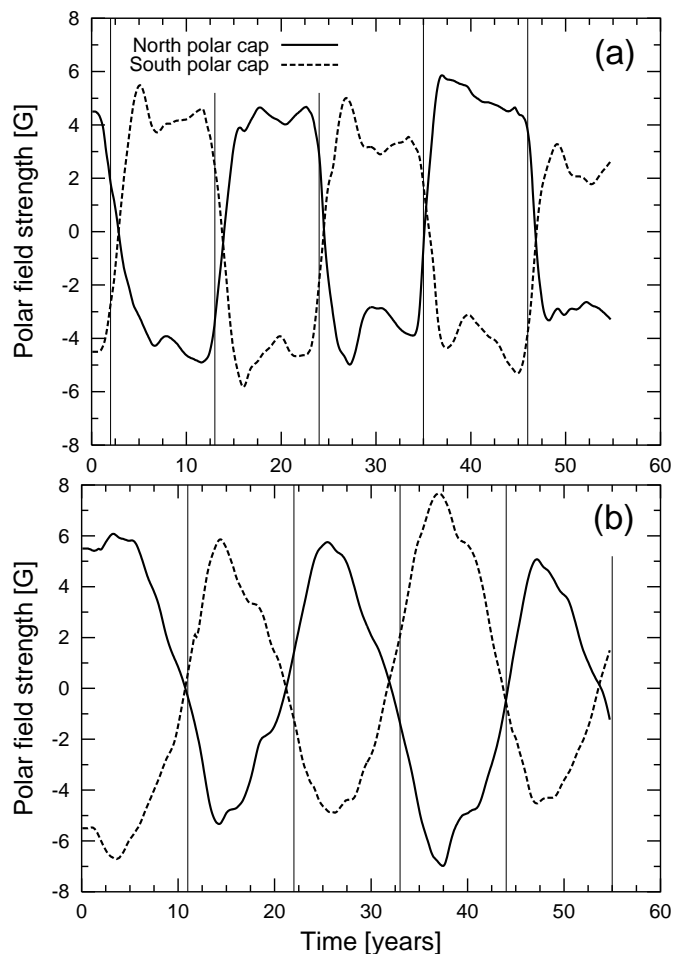


**Fig. 19.** Time evolution of the polar fields when the evolution of the emergence rate is described by 2 straight lines. The activity maximum, marked by the vertical lines, is reached after **a)** 2 years and after **b)** 11 years, respectively.

## References

- Bogart, R. S. 1987, *Sol. Phys.*, 110, 23  
 DeVore, C. R., & Sheeley, N. R. 1987, *Sol. Phys.*, 108, 47  
 DeVore, C. R., Boris, J. P., & Sheeley, N. R. 1984, *Sol. Phys.*, 92, 1  
 DeVore, C. R., Boris, J. P., Young, T. R., Sheeley, N. R., & Harvey, K. L. 1985a, *Aust. J. Phys.*, 38, 999  
 DeVore, C. R., Sheeley, N. R., Boris, J. P., Young, T. R., & Harvey, K. L. 1985b, *Sol. Phys.*, 102, 41  
 Duvall, T. L. 1979, *Sol. Phys.*, 63, 3  
 Harvey, K. L. 1992, in *The Solar Cycle*, ASP Conf. Ser., 27, 335  
 Harvey, K. L., & Zwaan, C. 1993, *Sol. Phys.*, 148, 85  
 Harvey-Angle, K. 1993, Ph.D. Thesis, Astronomical Inst. Utrecht Univ.  
 Hathaway, D. H. 1996, *ApJ*, 460, 1027  
 Hathaway, D. H., Wilson, R. M., & Reichmann, E. J. 1994, *Sol. Phys.*, 151, 177  
 Leighton, R. B. 1964, *ApJ*, 140, 1547  
 Mackay, D. H., Priest, E. R., & Lockwood, M. 2002a, *Sol. Phys.*, 207, 291  
 Mackay, D. H., Priest, E. R., & Lockwood, M. 2002b, *Sol. Phys.*, 209, 287  
 Makarov, V. I., Tlatov, A. G., & Sivaraman, K. R. 2003, *Sol. Phys.*, 214, 41



- Martinez Pillet, V., Lites, B. W., & Skumanich, A. 1997, *ApJ*, 474, 810
- Mosher, J. M. 1977, Ph.D. Thesis, California Institute of technology Press, W. H., Flannery, B. P., Teukolsky, S. A., & Vetterling, W. T. 1992, *Numerical Recipes: The Art of Scientific Computing* (Cambridge (UK), New York) Cambridge University Press), 2nd ed.
- Schrijver, C. J. 2001, *ApJ*, 546, 475
- Schrijver, C. J., & Harvey, K. L. 1994, *Sol. Phys.*, 150, 1
- Schrijver, C. J., & Title, A. 2001, *ApJ*, 551, 1099
- Schrijver, C. J., Title, A. M., van Ballegoijen, A. A., Hagenaar, H. J., & Shine, R. A. 1997, *ApJ*, 487, 424
- Schüssler, M., & Solanki, S. K. 1992, *A&A*, 264, L13
- Schüssler, M., Caligari, P., Ferriz-Mas, A., Solanki, S. K., & Stix, M. 1996, *A&A*, 314, 503
- Sheeley, N. R., DeVore, C. R., & Boris, J. P. 1985, *Sol. Phys.*, 98, 219
- Smith, E. J., & Balogh, A. 1995, *Geophys. Res. Lett.*, 22, 3317
- Snodgrass, H. B. 1983, *ApJ*, 270, 288
- Snodgrass, H. B., & Dailey, S. B. 1996, *Sol. Phys.*, 163, 21
- Solanki, S. K. 1993, *Space Sci. Rev.*, 63, 1
- Solanki, S. K., Schüssler, M., & Fligge, M. 2000, *Nature*, 408, 445
- Solanki, S. K., Krivova, N. A., Schüssler, M., & Fligge, M. 2002a, *A&A*, 396, 1029
- Solanki, S. K., Schüssler, M., & Fligge, M. 2002b, *A&A*, 383, 706
- Svalgaard, L., Duvall, T. L., & Scherrer, P. H. 1978, *Sol. Phys.*, 58, 225
- Topka, K., Moore, R., Labonte, B. J., & Howard, R. 1982, *Sol. Phys.*, 79, 231
- van Ballegoijen, A. A., Cartledge, N. P., & Priest, E. R. 1998, *ApJ*, 501, 866
- Vilhu, O., & Rucinski, S. M. 1983, *A&A*, 127, 5
- Wang, Y.-M., & Sheeley, N. R. 1989, *Sol. Phys.*, 124, 81
- Wang, Y.-M., & Sheeley, N. R. 1992, *ApJ*, 392, 310
- Wang, Y.-M., Nash, A. G., & Sheeley, N. R. 1989a, *ApJ*, 347, 529
- Wang, Y.-M., Nash, A. G., & Sheeley, N. R. 1989b, *Science*, 245, 712
- Wang, Y.-M., Sheeley, N. R. J., & Lean, J. 2000, *Geophys. Res. Lett.*, 27, 621